tvst

Retina

Noninvasive Ophthalmic Imaging Measures Retinal Degeneration and Vision Deficits in *Ndufs4*$^{-/-}$ Mouse Model of Mitochondrial Complex I Deficiency

Maria I. Avrutsky[1], Jacqueline M. Lawson[1], Jade E. Smart[1], Claire W. Chen[1], and Carol M. Troy[1–3]

[1] Department of Pathology and Cell Biology, Vagelos College of Physicians and Surgeons, Columbia University, New York, NY, USA
[2] Department of Neurology, Vagelos College of Physicians and Surgeons, Columbia University, New York, NY, USA
[3] The Taub Institute for Research on Alzheimer's Disease and the Aging Brain, Vagelos College of Physicians and Surgeons, Columbia University, New York, NY, USA

Correspondence: Carol M. Troy, 650 W 168th St. New York, NY 10032, USA. e-mail: cmt2@cumc.columbia.edu

Received: December 7, 2021
Accepted: July 7, 2022
Published: August 3, 2022

Keywords: retina; mitochondria; *Ndufs4*; optical coherence tomography; electroretinogram; optomotor reflex; complex I deficiency; neurodegeneration

Citation: Avrutsky MI, Lawson JM, Smart JE, Chen CW, Troy CM. Noninvasive ophthalmic imaging measures retinal degeneration and vision deficits in *Ndufs4*$^{-/-}$ mouse model of mitochondrial complex i deficiency. Transl Vis Sci Technol. 2022;11(8):5, https://doi.org/10.1167/tvst.11.8.5

Purpose: To characterize postnatal ocular pathology in a *Ndufs4*$^{-/-}$ mouse model of complex I deficiency using noninvasive retinal imaging and visual testing.

Methods: *Ndufs4*$^{-/-}$ mice and wild-type (WT) littermates were analyzed at 3, 5, and 7 weeks postnatal. Retinal morphology was visualized by optical coherence tomography (OCT). OCT images were analyzed for changes in retinal thickness and reflectivity profiles. Visual function was assessed by electroretinogram (ERG) and optomotor reflex (OMR).

Results: *Ndufs4*$^{-/-}$ animals have normal OCT morphology at weaning and develop inner plexiform layer atrophy over weeks 5 to 7. Outer retinal layers show hyporeflectivity of the external limiting membrane (ELM) and photoreceptor ellipsoid zone (EZ). Retinal function is impaired at 3 weeks, with profound deficits in b-wave, a-wave, and oscillatory potential amplitudes. The b-wave and oscillatory potential implicit times are delayed, but the a-wave implicit time is unaffected. *Ndufs4*$^{-/-}$ animals have normal OMR at 3 weeks and present with increasing acuity and contrast OMR deficits at 5 and 7 weeks. Physiological thinning of inner retinal layers, attenuation of ELM reflectivity, and attenuation of ERG b- and a-wave amplitudes occur in WT C57BL/6 littermates between weeks 3 and 7.

Conclusions: Noninvasive ocular imaging captures early-onset retinal degeneration in *Ndufs4*$^{-/-}$ mice and is a tractable approach for investigating retinal pathology subsequent to complex I deficiency.

Translational Relevance: Ophthalmic imaging captures clinically relevant measures of retinal disease in a fast-progressing mouse model of complex I deficiency consistent with human Leigh syndrome.

Introduction

Mitochondrial complex I disorders are a heterogeneous group of rare inherited diseases caused by mutations affecting proteins in the mitochondrial electron transport chain. Mutations disrupting complex I function account for up to 30% of inherited mitochondrial disorders,[1] including >95% of Leber's hereditary optic neuropathy[2] and >50% of Leigh syndrome cases.[3] Disease presentation and symptom severity can vary widely, from lethal neonatal disease (e.g., Leigh syndrome) to aging-related neurodegenerative disorders such as Parkinson's disease[4,5] and amyotrophic lateral sclerosis.[6] However, neurological and ophthalmic pathologies are common to many forms of complex I deficiency, due to the high energy demands of central nervous system tissues.

Copyright 2022 The Authors

This work is licensed under a Creative Commons Attribution-NonCommercial-NoDerivatives 4.0 International License.

Downloaded from hwmaint.iovs.org on 04/24/2024

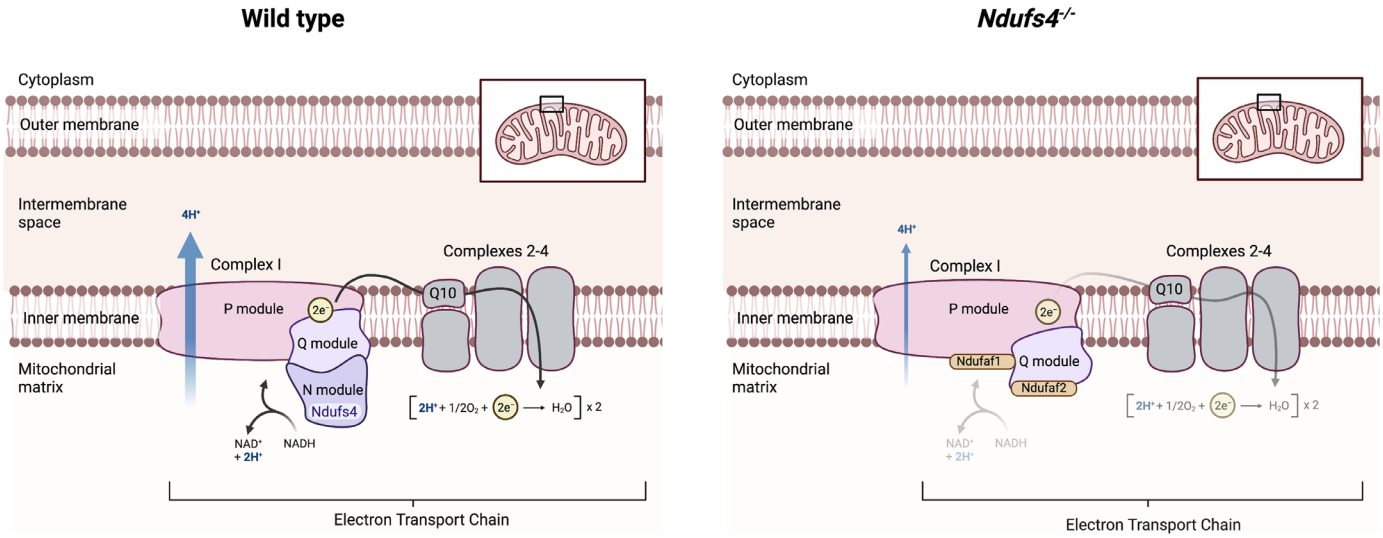

Figure 1. *Ndufs4*$^{-/-}$ model of complex I deficiency. Schematic shows how *Ndufs4* deficiency impairs complex I assembly and mitochondrial electron transport chain function. *Ndufs4* is a subunit of complex I, which catalyzes the transfer of electrons from NADH to coenzyme Q10 and helps establish the mitochondrial membrane potential by pumping H^+ ions across the inner mitochondrial membrane. In *Ndufs4*$^{-/-}$ cells, the N module failed to assemble, and complex I remained errantly associated with assembly factors NDUFAF1 (NADH:ubiquinone oxidoreductase complex assembly factor 1) and NDUFAF2 (NADH:ubiquinone oxidoreductase complex assembly factor 2). Figure made with BioRender.com.

Mammalian complex I (also known as NADH:ubiquinone oxidoreductase) is the first and largest of five mitochondrial complexes in the electron transport chain,[7] which generates cellular energy via oxidative phosphorylation of adenosine triphosphate (Fig. 1). The complex is composed of 44 different subunits, which are organized into three functional modules (N module, Q module, and P module).[8] The N module mediates binding and oxidizing of NADH, the Q module catalyzes the transfer of electrons from NADH to coenzyme Q10, and the P module helps establish the mitochondrial membrane potential by pumping H^+ ions across the inner mitochondrial membrane. Complex I deficiencies destabilize mitochondrial oxidative phosphorylation, resulting in devastating energy production deficits.[9]

NADH:ubiquinone oxidoreductase Fe-S protein 4 (*Ndufs4*) is a nuclear-encoded protein essential for complex I assembly and activity.[10,11] In cells lacking *Ndufs4* expression, complex I fails to assemble the N module (Fig. 1).[12,13] Patients with *Ndufs4* loss-of-function mutations develop Leigh syndrome, a fatal pediatric disorder characterized by severe mitochondrial energy generation deficits.[14–17] Patients typically present in infancy with elevated lactate in cerebral spinal fluid and serum, hypotonia, loss of vision, and progressive neurological dysfunction due to diminished complex I activity. Vision problems may include nystagmus, strabismus, ophthalmoplegia, and optic atrophy. Similarly, *Ndufs4* deficiency in mice results in diminished growth rate, hypothermia, ataxic signs, and elevated serum lactate.[10] Knockout animals develop progressive encephalomyopathy by around 5 weeks of age and die by 50 to 60 days postnatal. Ocular pathology in *Ndufs4*$^{-/-}$ animals recapitulates the neurological and ophthalmic features of human complex I deficiency, such as retinal neurodegeneration, inflammation, and visual function deficits. Due to the rapid and severe course of disease progression, the *Ndufs4*$^{-/-}$ mouse is an attractive model for testing therapeutic interventions that target retinal pathologies resulting from complex I deficiency.[11,18–21]

The timing of onset, rate of progression, and variability of ocular pathology in the *Ndufs4*$^{-/-}$ mouse remain poorly understood, in part due to conflicting reports from inadequately powered studies.[10,11,22] Although some retinal abnormalities have been observed in 2- to 3-week-old animals,[23] most investigations into *Ndufs4*$^{-/-}$ neurodegenerative ocular phenotypes use animals 5 to 7 weeks old. Ophthalmic live imaging by optical coherence tomography (OCT) and retinal functional testing by electroretinogram (ERG) enable noninvasive analysis of retinal pathology in living animals. These tools enable direct comparison of ophthalmic clinical readouts from human patients with relevant experimental animal models.[24] Here, we present a panel of noninvasive opthalmic measures of

translational vision science & technology

Downloaded from hwmaint.iovs.org on 04/24/2024

retinal pathology and visual dysfunction in *Ndufs4*$^{-/-}$ mice.

Methods

Animals

Ndufs4$^{-/-}$ animals (B6.129S4-Ndufs4tm1.1Rpa/J) are on a C57BL/6 background. Breeding *Ndufs4*$^{+/-}$ pairs were purchased from The Jackson Laboratory (Bar Harbor, ME). Male and female offspring from heterozygote breeding pairs were genotyped to select wild-type (WT) and knockout (*Ndufs4*$^{-/-}$) littermates for this study. Genotyping protocol was performed as directed by The Jackson Laboratory (primers: AGT CAG CAA CAT TTT GGC AGT, GAG CTT GCC TAG GAG GAG GT, AGG GGA CTG GAC TAA CAG CA). Three different cohorts of animals were weighed (Fig. 2A), and analyzed at 3 weeks postnatal (p21–p22), 5 weeks postnatal (p35–p36), or 7 weeks postnatal (p49–p50). Knockout morbidity and mortality precluded evaluation of animals older than 7 weeks. All investigations were performed in accordance with the ARVO Statement for the Use of Animals in Ophthalmic and Vision Research. Rodent experiments were approved and monitored by the Institutional Animal Care and Use Committee (IACUC) of Columbia University.

Histology and Eyecup Measurements

Mice were euthanized with intraperitoneal (IP) administration of overdose of ketamine (160–200 mg/kg) plus xylazine (10–20 mg/kg) and perfused with saline, followed by fixation with 4% paraformaldehyde. Eyes were enucleated, embedded in optimal cutting temperature compound, and cryosectioned at 20-µm per section. For hematoxylin and eosin (H&E) staining, slides were submitted to the Columbia University Medical Center Molecular Pathology Shared Resource Histology Service. Eye size measurements of 7-week-old mice were obtained from microscopy images of retinal sections from the medial horizontal plane of the eye. Ocular sections were imaged with a Nikon (Tokyo, Japan) microscope and SPOT digital camera (SPOT Imaging, Sterling Heights, MI). The diameter of each eyecup (L_x and L_y) was measured as depicted in Figure 2B, using FIJI image processing software. The measurements from six sections on each slide were averaged. Sections that greatly deviated from circularity were excluded from measurement.

Electroretinography

Animals were dark adapted for 2 to 16 hours and handled under deep-red light-emitting diode (LED) lighting to preserve dark adaptation. Animals received tropicamide and phenylephrine chloride eyedrops to dilate the pupil (pupil size was not measured) and were anesthetized with IP administration of ketamine (80–100 mg/kg) and xylazine (5–10 mg/kg). Focal ERGs were recorded with the MICRON IV Image-Guided Focal ERG System (Phoenix Research Industries, Duluth, GA), using a flash spot size of 1.5 mm, centered on the optic nerve head, and 10-ms white light LED stimulus intensities of −0.7, 1.1, and 2.3 log (cd·s/m^2). The 1.5-mm flash spot size was selected as it is the largest diameter of stimulus available for the MICRON IV Focal ERG System. A 650-nm deep-red light filter was used to preserve dark adaptation while positioning the eye in contact with the corneal electrode and centering the flash stimulus directly on the retina (Fig. 2D). At each stimulus intensity, 10 ERG traces were recorded, with a 5-second break between each recording and a 30-second break before each increase in stimulus intensity. A sham reading (no light stimulus) was recorded immediately prior to exposure to light stimulus. Amplitudes and implicit times of the a- and b-waves and oscillatory potentials (OPs) were calculated using LabScribe 3 ERG automated software (iWorx Systems, Dover, NH). OPs were derived using a 30- to 300-Hz filter, and the sum of the first six OPs was used to calculate the sum OP amplitude. Waveform amplitude measurements derived from sham recordings were subtracted from all amplitudes calculated by LabScribe 3 ERG for that eye, to account for background noise in focal ERG traces.

Optical Coherence Tomography

OCT imaging was performed using the Phoenix MICRON IV Image-Guided OCT System. Animals received tropicamide and phenylephrine chloride eyedrops to dilate the pupil and were anesthetized with IP administration of ketamine (80–100 mg/kg) and xylazine (5–10 mg/kg). For each eye, two vertical and two horizontal OCT scans (longitudinal resolution, 1.8 µm; transverse resolution, 3 µm; scan length, 1625 µm; average of 30 frames/scan) were captured approximately 400 µm from the optic nerve (Fig. 2E). Imaging was performed by investigators masked to genotype, and animals with congenital retinal defects or corneal opacities that impair OCT acquisition (Figs. 2F, 2G) were eliminated from evaluation.

Four OCT images per eye were averaged to generate mean retinal thickness values. Segmentation of

translational vision science & technology

Downloaded from hwmaint.iovs.org on 04/24/2024

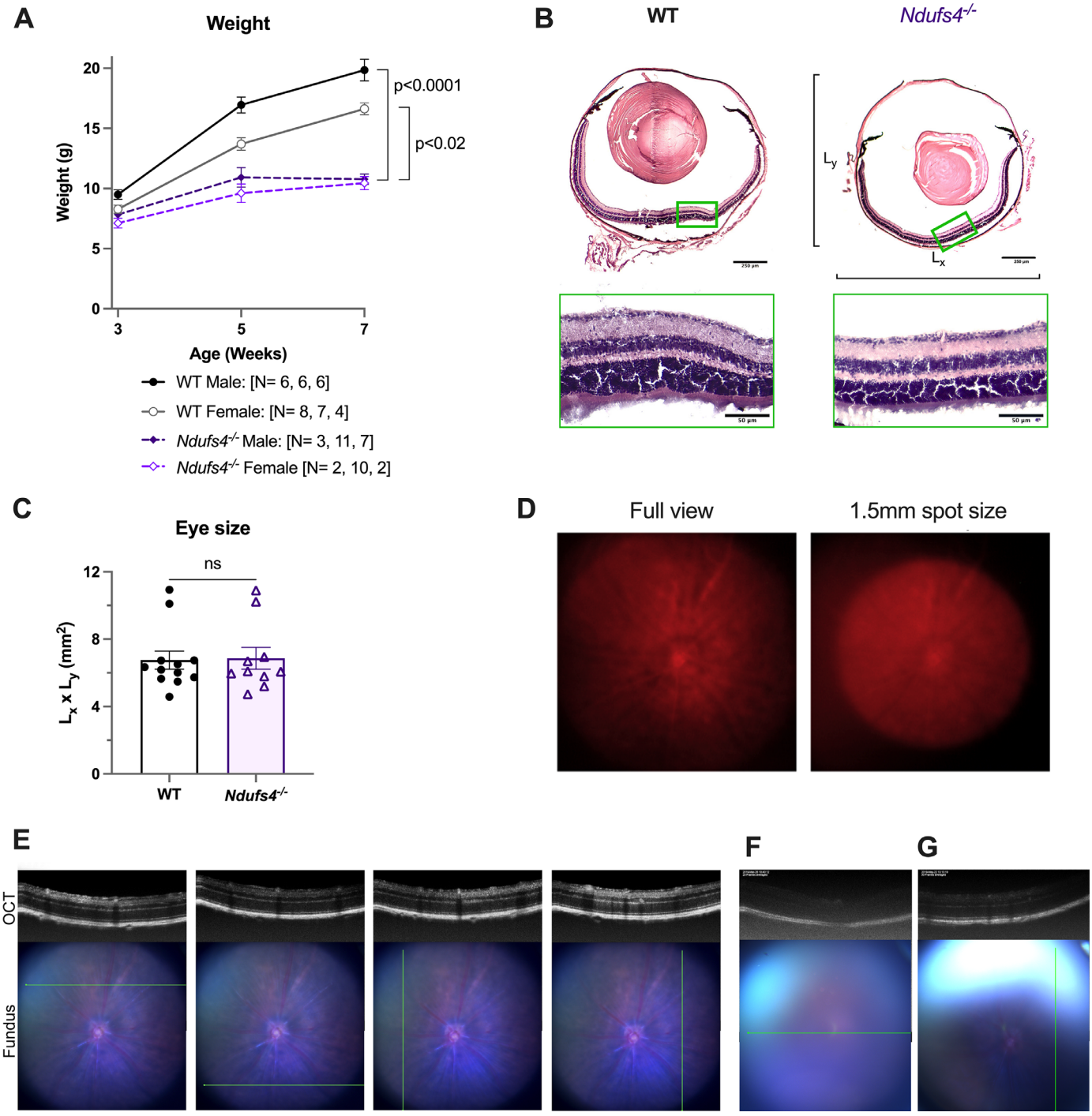

Figure 2. Animal weights and ophthalmic imaging parameters. (**A**) Weight (in grams) of *Ndufs4*$^{-/-}$ (*n* for each genotype is indicated in the legend at 3, 5, and 7 weeks). Data are presented as mean ± SEM. Differences between groups were analyzed by two-way ANOVA, followed by Tukey's multiple comparisons test. (**B**) Representative H&E staining of ocular sections from 7-week-old WT and *Ndufs4*$^{-/-}$ littermates. *Scale bars*: 250 µm (*main image*) and 50 µm (*inset*). Schema demonstrate ocular dimension measurements L_y and L_x. (**C**) Quantification of ocular dimensions (measured as $L_x \times L_y$) of WT ($n = 12$) and *Ndufs4*$^{-/-}$ ($n = 10$) eyes at week 7. Differences between groups were evaluated by unpaired *t*-test. (**D**) Representative view of ocular positioning and 1.5-mm spot size for ERG recording. (**E**) Representative fundus and OCT imaging demonstrates the positioning of four OCT scans in the same eye. The location of each OCT scan is indicated by a *green line* on the associated fundus image. (**F**) Representative image of excessive corneal opacity that precludes OCT layer thickness analysis. (**G**) Representative image of corneal opacity that is acceptable for OCT measurement of retinal layer thicknesses but precludes evaluation of outer retinal reflectivity.

Downloaded from hwmaint.iovs.org on 04/24/2024

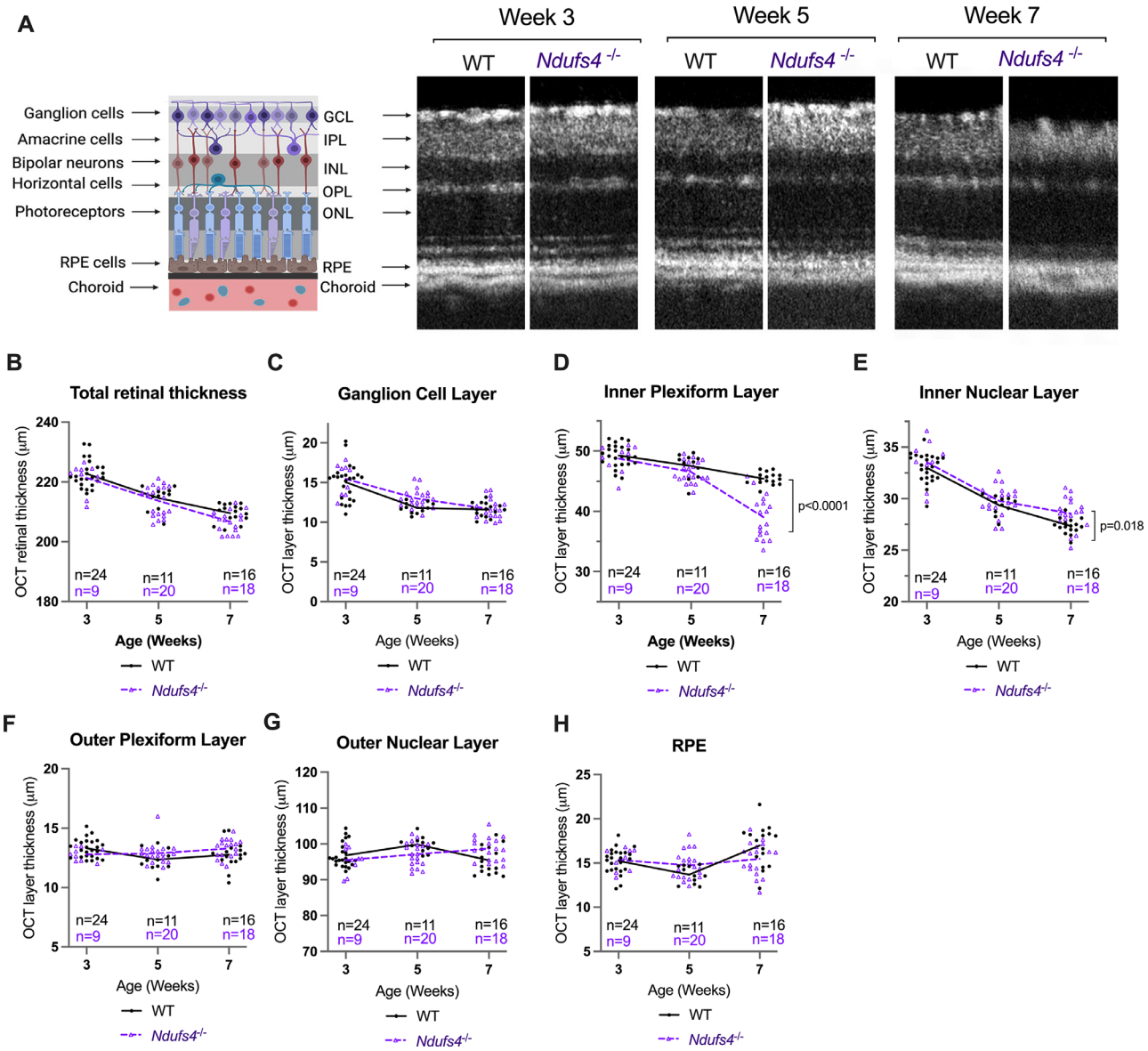

Figure 3. OCT imaging reveals IPL atrophy in 7-week-old *Ndufs4*$^{-/-}$ mice. (**A**) Schematic diagram (made with Biorender.com) depicting neuronal distribution in different retinal layers and representative OCT images of WT and *Ndufs4*$^{-/-}$ littermates at 3, 5, and 7 weeks. (B–H) The total retinal (**B**), GCL (**C**), IPL (**D**), INL (**E**), OPL (**F**), outer nuclear layer (ONL) (**G**), and RPE (**H**) thickness in WT and *Ndufs4*$^{-/-}$ eyes at 3, 5, and 7 weeks. Data are presented as mean ± SEM (*n* at each timepoint is indicated on the graphs). Differences between groups were analyzed by two-way ANOVA, followed by Tukey's multiple comparisons test. Multiple comparisons plots are shown in Supplementary Figure S1. IS/OS, inner segment/outer segment.

individual retinal layers was generated using Phoenix MICRON OCT Segmentation software, and average layer thicknesses were calculated in Excel (Microsoft Corporation, Redmond, WA). Specific retinal layers were identified as indicated in Figure 3A. Total retinal thickness was measured from the ganglion cell layer (GCL) to the retinal pigment epithelium (RPE).

For reflectivity analysis, a 200 × 200-µm region of interest selection centered on the RPE layer was analyzed using FIJI Analyze>Plot Profile to generate a numerical reflectivity profile. Peak reflectivity values of each outer retinal band were normalized against the reflectivity of the outer nuclear layer, and quantifications from four OCT images were averaged for each eye. All OCT image processing was performed by an investigator who was masked to the genotype of the animals analyzed.

Optomotor Reflex

Contrast sensitivity and visual acuity were measured using the OptoDrum automated optomotor reaction

translational vision science & technology

Downloaded from hwmaint.iovs.org on 04/24/2024

system (Striatech GmbH, Tübingen, Germany).[25] Animals were handled by a trained investigator to avoid overactivity and monitored for attentiveness during the imaging sessions. Optomotor reflexes were recorded by an automated tracking system, and limits of visual perception were determined by increasing the spatial frequency (acuity measure) or decreasing the contrast (contrast measure) of the stimulus until an animal failed to respond to the stimulus on two consecutive trials.

Statistics

Data were analyzed using Excel and Prism (GraphPad Software, San Diego, CA). Statistical tests, n values, and P values are described in the figures and legends. Data are presented as mean ± SEM. The n value at each timepoint is indicated on the graphs. Differences between groups were analyzed by two-way analysis of variance (ANOVA), followed by Tukey's multiple comparisons test. Correlation analysis was performed by linear regression. Significance was defined as $P < 0.05$. No statistical methods were used to predetermine sample size.

Results

Retinal Thickness Changes in Postnatal WT and *Ndufs4*$^{-/-}$ Animals

Ndufs4$^{-/-}$ mice have weights similar to those of their WT littermates at 3 weeks of age (Fig. 2A). From 3 to 7 weeks of age, the weight of WT male and female mice increases by 200%, but the weight of *Ndufs4*$^{-/-}$ animals increases by only 50%. By 5 weeks, *Ndufs4*$^{-/-}$ animals are significantly smaller than their WT littermates. H&E staining of ocular sections revealed typical retinal layer morphology in 7-week-old animals (Fig. 2B), and measurements of eye-cup diameters showed no differences between WT and *Ndufs4*$^{-/-}$ eyes (Fig. 2C).

OCT imaging showed normal retinal morphology and no genotype-dependent differences in retinal layer thicknesses in 3- to 5-week-old knockout animals (Fig. 3, Supplementary Fig. S1). At 7 weeks, the inner plexiform layer (IPL) of *Ndufs4*$^{-/-}$ animals was 14.1% thinner (95% confidence interval [CI], 9.2–19.0) compared to WT littermates (Figs. 3A, 3D). We also observed a modestly thicker inner nuclear layer (INL) in *Ndufs4*$^{-/-}$ mice compared to WT ($P = 0.018$, ANOVA) (Fig. 3E); however, the effect did not retain statistical significance by multiple comparisons testing of age-matched animals (Supplementary Fig. S1). Postnatal retinal remodeling of the GCL, IPL, and INL results in a 6.3% decrease (95% CI, 4.1–8.9) in total retinal thickness in both WT and knockout animals over weeks 3 to 7 (Figs. 3A–3E). The outer retina and RPE did not show any genotype-dependent or age-dependent thickness changes during this time period (Figs. 3F–3H).

Outer Retinal Reflectivity Abnormalities in *Ndufs4*$^{-/-}$ Mice

The outer retinal region of the OCT contains four high-reflectivity bands, corresponding to the external limiting membrane (ELM), the inner/outer segments of the photoreceptors (ellipsoid zone [EZ]), the RPE, and the choriocapillaris (CC) (Fig. 4A). Quantitative evaluation of outer retinal band reflectivity requires high-quality OCT imaging to determine the resolution of these bands; corneal opacities such as those shown in Figure 2G result in reduced OCT image quality that is not qualified for reflectivity analysis. Although reflectivity of inner retinal layers was highly variable (Fig. 2E), outer retinal reflectivity was generally consistent among different OCT scans. ELM reflectivity was brightest in 3-week-old animals; by 7 weeks of age, ELM reflectivity decreased by 8.0% (95% CI, 1.3–14.8) in WT animals and by 11.4% (95% CI, 2.6–20.2) in *Ndufs4*$^{-/-}$ animals (Fig. 4B, Supplementary Fig. S2). *Ndufs4*$^{-/-}$ animals had significantly reduced ELM reflectivity compared to WT animals ($P = 0.0003$, ANOVA). Reflectivity differences between knockout and WT animals became more apparent at 5 weeks (Table); however, differences between groups did not reach statistical significance by multiple comparisons testing at specific timepoints.

EZ reflectivity was also markedly reduced in 5- to 7-week-old *Ndufs4*$^{-/-}$ animals (Fig. 4C). *Ndufs4*$^{-/-}$ mice had 20.3% (95% CI, 4.5–36.2) and 23.7% (95% CI, 8.5–38.9) lower EZ reflectivity compared to WT littermates at 5 and 7 weeks of age, respectively. EZ reflectivity did not show significant age-dependent changes (Supplementary Fig. S2); however, differences between genotypes were more apparent in older animals compared to 3-week-old mice. These reflectivity abnormalities are specific to the ELM and EZ bands; we did not observe any age-dependent or genotype-dependent differences in the reflectivity of the RPE or CC bands (Figs. 4D, 4E). Because the reflectivity of outer retinal bands on OCT could be influenced by age-dependent changes in inner retinal thickness, we measured the correlation between ELM or EZ reflectivity and the thickness of the inner retinal layers (retinal ganglion cell [RGC] + IPL + INL) or

translational vision science & technology

Downloaded from hwmaint.iovs.org on 04/24/2024

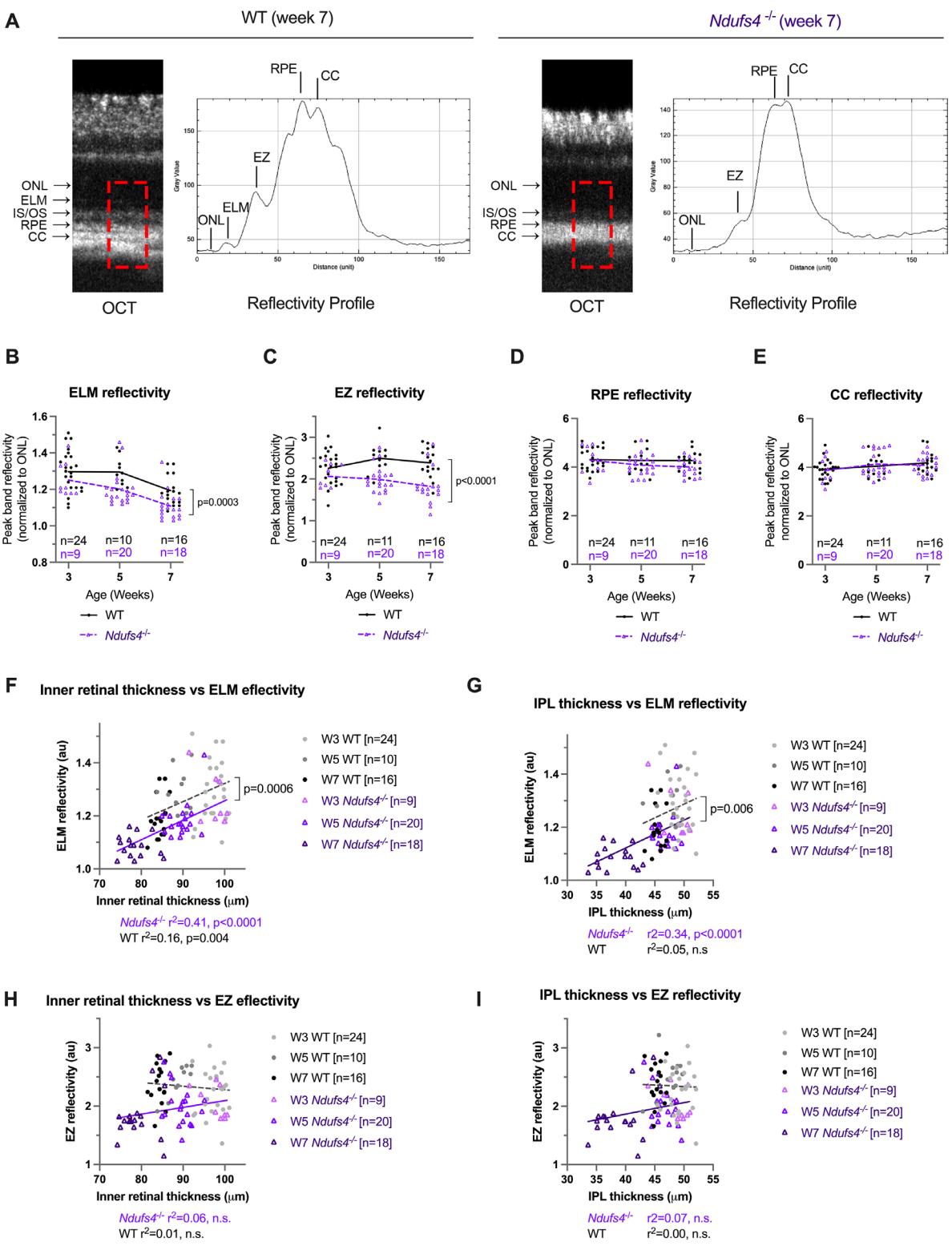

Figure 4. Outer retinal hyporeflectivity in *Ndufs4*$^{-/-}$ mice. (**A**) Representative OCT images and reflectivity profiles of hyperreflective outer retinal bands in WT and *Ndufs4*$^{-/-}$ littermates. (B–E) The ELM (**B**), EZ (**C**), RPE (**D**), and CC (**E**) reflectivity in WT and *Ndufs4*$^{-/-}$ eyes at 3, 5, and 7 weeks (*n* at each timepoint is indicated on the graphs). Data are presented as mean ± SEM. Differences between groups were analyzed by two-way ANOVA, followed by Tukey's multiple comparisons test. One W5 WT outlier removed by Grubbs' outlier test is shown in (**B**). Multiple comparisons plots are shown in Supplementary Figure S2. (**F**) Linear regression between inner retinal thickness and ELM reflectivity in WT and *Ndufs4*$^{-/-}$ retinas. (**G**) Linear regression between IPL thickness and ELM reflectivity in WT and *Ndufs4*$^{-/-}$ retinas. (**H**) Linear regression between inner retinal thickness and EZ reflectivity in WT and *Ndufs4*$^{-/-}$ retinas. (**I**) Linear regression between IPL thickness and EZ reflectivity in WT and *Ndufs4*$^{-/-}$ retinas.

translational vision science & technology

Downloaded from hwmaint.iovs.org on 04/24/2024

Table. Summary of Observed *Ndufs4*$^{-/-}$ Ocular Phenotypes and Power Analysis

Phenotype	Week 3	Week 5	Week 7
ERG: b-wave			
Flash: 2.3 log (cd·s/m^2)			
WT (μV), mean (SD)	225.7 (77.0)	150.1 (60.0)	235.8 (101.4)
Ndufs4$^{-/-}$ (μV), mean (SD)	127.5 (53.8)	60.1 (50.2)	88.4 (62.2)
Power: *Ndufs4*$^{-/-}$ vs. WT,[a] *n*	7	6	5
Power: 50% improvement,[b] *n*	19	20	17
ERG: a-wave			
Flash: 2.3 log (cd·s/m^2)			
WT (μV), mean (SD)	−107.2 (40.3)	−59.5 (23.1)	−104.3 (43.0)
Ndufs4$^{-/-}$ (μV), mean (SD)	−70.4 (33.6)	−34.5 (25.3)	−45.7 (27.2)
Power: *Ndufs4*$^{-/-}$ vs. WT,[a] *n*	16	15	6
Power: 50% improvement,[b] *n*	52	68	13
ERG: OP			
Flash: 2.3 log (cd·s/m^2)			
WT (μV), mean (SD)	133.8 (76.2)	109.6 (68.4)	173.7 (109.6)
Ndufs4$^{-/-}$ (μV), mean (SD)	72.4 (61.5)	25.5 (29.6)	39.6 (41.5)
Power: *Ndufs4*$^{-/-}$ vs. WT,[a] *n*	20	5	5
Power: 50% improvement,[b] *n*	54	8	9
ERG: OP_1			
Flash: 2.3 log (cd·s/m^2)			
WT (μV), mean (SD)	40.2 (19.4)	37.7(19.5)	46.3 (32.4)
Ndufs4$^{-/-}$ (μV), mean (SD)	19.8 (15.51)	7.6 (7.9)	12.9 (12.8)
Power: *Ndufs4*$^{-/-}$ vs. WT,[a] *n*	12	<5	<5
Power: 50% improvement,[b] *n*	37	5	10
OCT: IPL			
WT (μm), mean (SD)	49.3 (1.8)	47.5 (2.1)	45.4 (1.0)
Ndufs4$^{-/-}$ (μm), mean (SD)	48.8 (2.4)	46.5 (1.9)	39.1 (3.6)
Power: *Ndufs4*$^{-/-}$ vs. WT,[a] *n*	—	57	<5
Power: 50% improvement,[b] *n*	—	>100	20
OCT: ELM reflectivity			
WT (a.u.), mean (SD)	1.30 (0.11)	1.3 (0.08)	1.19 (0.08)
Ndufs4$^{-/-}$ (a.u.), mean (SD)	1.25 (0.09)	1.20 (0.09)	1.11 (0.08)
Power: *Ndufs4*$^{-/-}$ vs. WT,[a] *n*	63	11	16
Power: 50% improvement,[b] *n*	>100	54	61
OCT: EZ reflectivity			
WT (a.u.), mean (SD)	2.26 (0.39)	2.50 (0.35)	2.39 (0.35)
Ndufs4$^{-/-}$ (a.u.), mean (SD)	2.06 (0.28)	1.99 (0.33)	1.82 (0.41)
Power: *Ndufs4*$^{-/-}$ vs. WT,[a] *n*	44	7	7
Power: 50% improvement,[b] *n*	>100	27	31
OMR: acuity			
WT (cycles/degree), mean (SD)	160.6 (16.4)	148.7 (16.4)	154.4 (14.9)
Ndufs4$^{-/-}$ (cycles/degree), mean (SD)	158.0 (13.0)	125.7 (16.2)	83.3 (58.5)
Power: *Ndufs4*$^{-/-}$ vs. WT,[a] *n*	—	8	<5
Power: 50% improvement,[b] *n*	—	31	42
OMR: contrast			
WT (% contrast), mean (SD)	4.0 (3.9)	4.8 (1.7)	2.7 (2.3)
Ndufs4$^{-/-}$ (% contrast), mean (SD)	4.6 (2.5)	12.2 (15.5)	58.7 (49.1)
Power: *Ndufs4*$^{-/-}$ vs. WT,[a] *n*	—	11	<5
Power: 50% improvement,[b] *n*	—	>100	48

Summary *Ndufs4*$^{-/-}$ ocular pathologies captured by OCT imaging, ERG imaging, and OMR testing. Power analysis is based on a normal distribution, two-sided test ($\alpha = 0.05$; power, 0.8).

[a]Power analysis (*n*/group) for distinguishing between *Ndufs4*$^{-/-}$ and WT littermate mice.

[b]Power analysis (*n*/group) for detecting a therapeutic effect that reduces pathology by 50%.

Downloaded from hwmaint.iovs.org on 04/24/2024

IPL specifically. ELM reflectivity declines were significantly correlated with inner retinal (Fig. 4F) and IPL (Fig. 4G) thinning in both WT and *Ndufs4*$^{-/-}$ animals. *Ndufs4*$^{-/-}$ ELM reflectivity deficits were still apparent after controlling for genotype-specific differences in retinal thickness. Conversely, EZ bands, which do not exhibit age-dependent changes in reflectivity, were also not correlated with changes in retinal thickness (Figs. 4H, 4I).

Ndufs4$^{-/-}$ ERG Deficits Are Present at Weaning

The two principal measures of the ERG waveform are the a-wave amplitude, which reflects phototransduction by photoreceptors, and the b-wave amplitude, which is generated by cells postsynaptic to the photoreceptors,[26] with contributions from bipolar cells, Müller glia, horizontal cells, and amacrine cells.[27] OPs are the oscillations appearing on the rising phase of the b-wave, and they are thought to arise from interactions among bipolar cells, amacrine cells, and ganglion neurons[27] (Fig. 5A). Although some *Ndufs4*$^{-/-}$ mice had profound ERG deficits from weaning, the penetrance of these deficits was more variable in younger animals (Fig. 5, Supplementary Fig. S3). Some 3-week-old *Ndufs4*$^{-/-}$ animals had normal ERG readings, whereas others were severely impaired. On average, 3-week-old knockout mice had 43.5% weaker (95% CI, 8.5–78.6) b-wave amplitudes compared to WT mice (Fig. 5A, B). Although there was no statistically significant age-dependent decrease in *Ndufs4*$^{-/-}$ ERG function, genotype-specific differences were better resolved after week 5. By 7 weeks, *Ndufs4*$^{-/-}$ mice had 56.2% weaker (95% CI, 22.3–90.2) a-wave amplitudes and 62.6% weaker (95% CI, 31.1–93.9) b-wave amplitudes compared to WT mice (Figs. 5A–5C).

The b-wave was generally more affected than the a-wave, as evidenced by the lower b/a ratio in the *Ndufs4*$^{-/-}$ animals (Fig. 5D). At 5 weeks of age, 37% of *Ndufs4*$^{-/-}$ animals had nearly complete absence of ERG b-wave response (b-wave amplitude $< 25\,\mu V$), and 25% of *Ndufs4*$^{-/-}$ animals had no measurable a-wave. Likewise, the amplitudes of the OPs were substantially weaker in *Ndufs4*$^{-/-}$ animals compared to WT animals. The first OP positive inflection (OP_1) was 79.9% lower (95% CI, 29.8–100.0) in 5-week-old *Ndufs4*$^{-/-}$ animals compared to WT animals (Fig. 5E). Meanwhile, the sum of the first six oscillatory potential amplitudes (Sum6OP) was 76.8% lower (95% CI, 12.4–100.0) in *Ndufs4*$^{-/-}$ animals compared to WT (Fig. 5F).

Delays in OP and b-wave implicit times reveal compounding defects in retinal electrophysiology downstream of photoreceptor phototransduction. These deficits were genotype dependent and not age dependent. The a-wave implicit time was unaffected (Fig. 5G). The OP_1 implicit time was modestly delayed ($P = 0.002$, ANOVA), although these differences were not significant by multiple comparisons testing of age-matched animals (Fig. 5H, Supplementary Fig. S3). Meanwhile, the b-wave implicit was delayed by 46.3 ms (95% CI, 21.5–71.1) in 5-week-old *Ndufs4*$^{-/-}$ animals (Fig. 4I).

ERG Deficits in *Ndufs4*$^{-/-}$ Mice Correlate With Inner Retinal Atrophy

We next evaluated the relationships between different ERG parameters by linear regression. The b- and a-wave amplitudes were highly correlated, consistent with the method of b-wave quantification, which measures b-wave amplitude from peak negative a-wave deflection (Fig. 6a). The lower *y*-intercept for *Ndufs4*$^{-/-}$ linear regression compared to WT indicates that b-wave amplitudes are more severely affected than a-wave amplitudes, consistent with the reduced b/a amplitude ratio quantifications (Fig. 5D). Because *Ndufs4*$^{-/-}$ b-wave amplitudes and implicit time annotations can be confounded by their diminished oscillatory potentials, we investigated the correlation between b-wave amplitude and OP_3 (the third OP, which overlaps the peak of the b-wave) (Fig. 6B). The b-wave amplitudes were significantly correlated with OP_3 measurements, and the slopes of the linear regressions for WT and *Ndufs4*$^{-/-}$ mice were not significantly different. If the primary reason for diminished b-wave amplitude in *Ndufs4*$^{-/-}$ mice was due to a confounding effect from a diminished OP response, we would expect the two linear regression lines to be closely superimposed. Instead, the *y*-intercept for *Ndufs4*$^{-/-}$ mice was significantly lower than the *y*-intercept for WT mice ($P < 0.0001$), indicating that the profound deficit in *Ndufs4*$^{-/-}$ OPs is not sufficient to explain the observed b-wave amplitude deficits. Measurement of b-wave implicit time was also significantly correlated with OP_3 (Fig. 6C). The b-wave amplitudes were also significantly correlated with b-wave implicit times, with extreme delays (implicit times >100 ms) exclusively occurring in animals with severely impaired b-wave (Fig. 6D). The slopes of linear regressions between b-wave amplitude and b-wave implicit time were significantly steeper for *Ndufs4*$^{-/-}$ compared to WT animals ($P < 0.0001$), indicating that *Ndufs4* deficiency resulted in more severe b-wave implicit time

translational vision science & technology

Downloaded from hwmaint.iovs.org on 04/24/2024

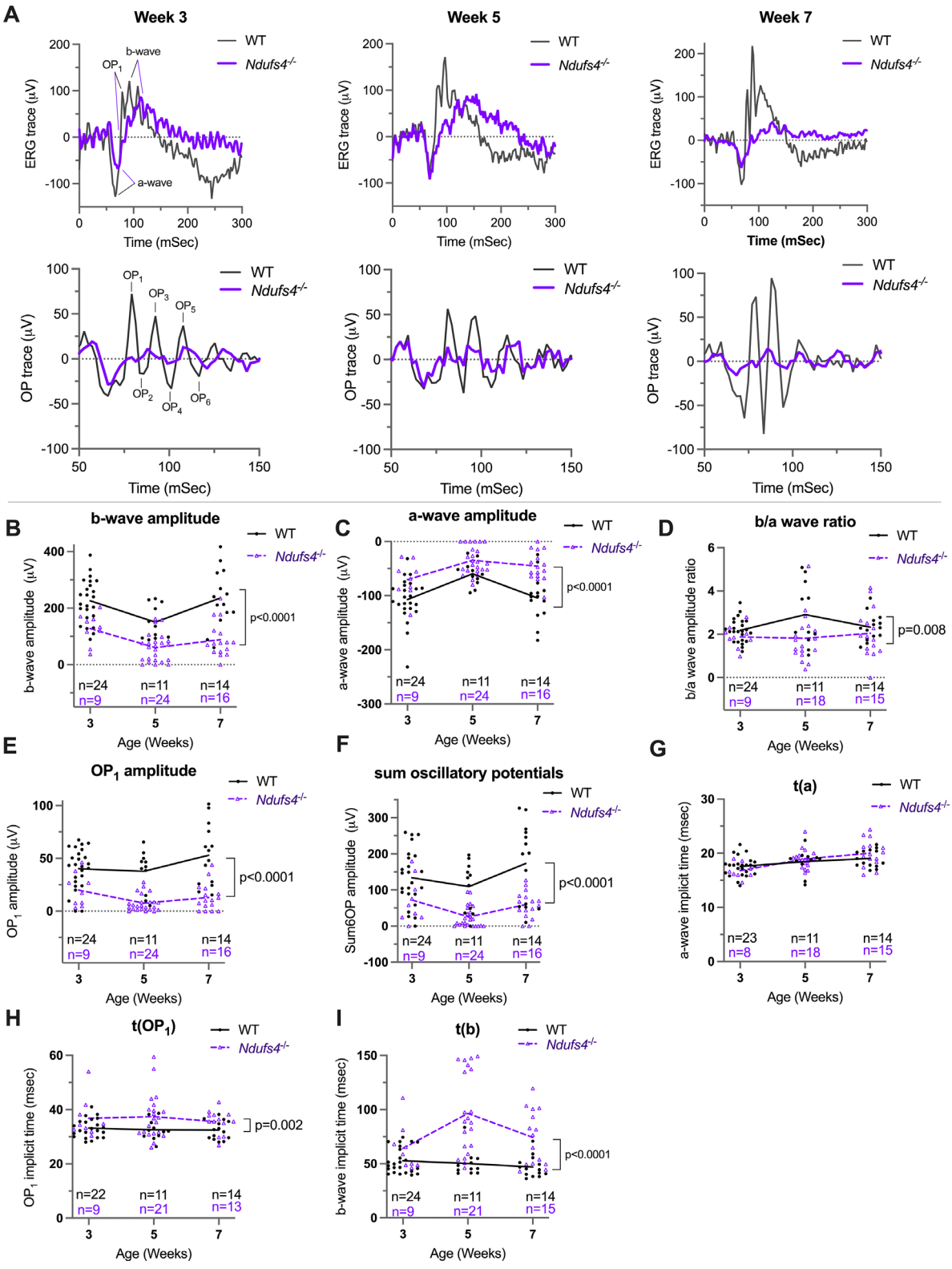

Figure 5. ERG deficits measure functional impairment in *Ndufs4*$^{-/-}$ mice. (**A**) Representative ERG traces (*top*) and OP traces (*bottom*) in 3-, 5-, and 7-week-old littermates showed attenuated a-wave, b-wave, and OP amplitudes and delayed b-wave implicit times in *Ndufs4*$^{-/-}$ mice. (**B**–**I**) The b-wave amplitude (**B**), a-wave amplitude (**C**), b/a ratio (**D**), OP_1 amplitude (**E**), sum oscillatory potentials amplitude (**F**), a-wave implicit time (**G**), OP_1 implicit time (**H**), and b-wave implicit time (**I**) measurements in WT and *Ndufs4*$^{-/-}$ littermates at 3, 5, and 7 weeks (*n* at each timepoint is indicated on the graphs). Data are presented as mean ± SEM. Differences between groups were analyzed by two-way ANOVA, followed by Tukey's multiple comparisons test. One W3 *Ndufs4*$^{-/-}$ outlier removed by Grubbs' outlier test is shown in (**G**). Multiple comparisons plots are shown in Supplementary Figure S3.

translational vision science & technology

Downloaded from hwmaint.iovs.org on 04/24/2024

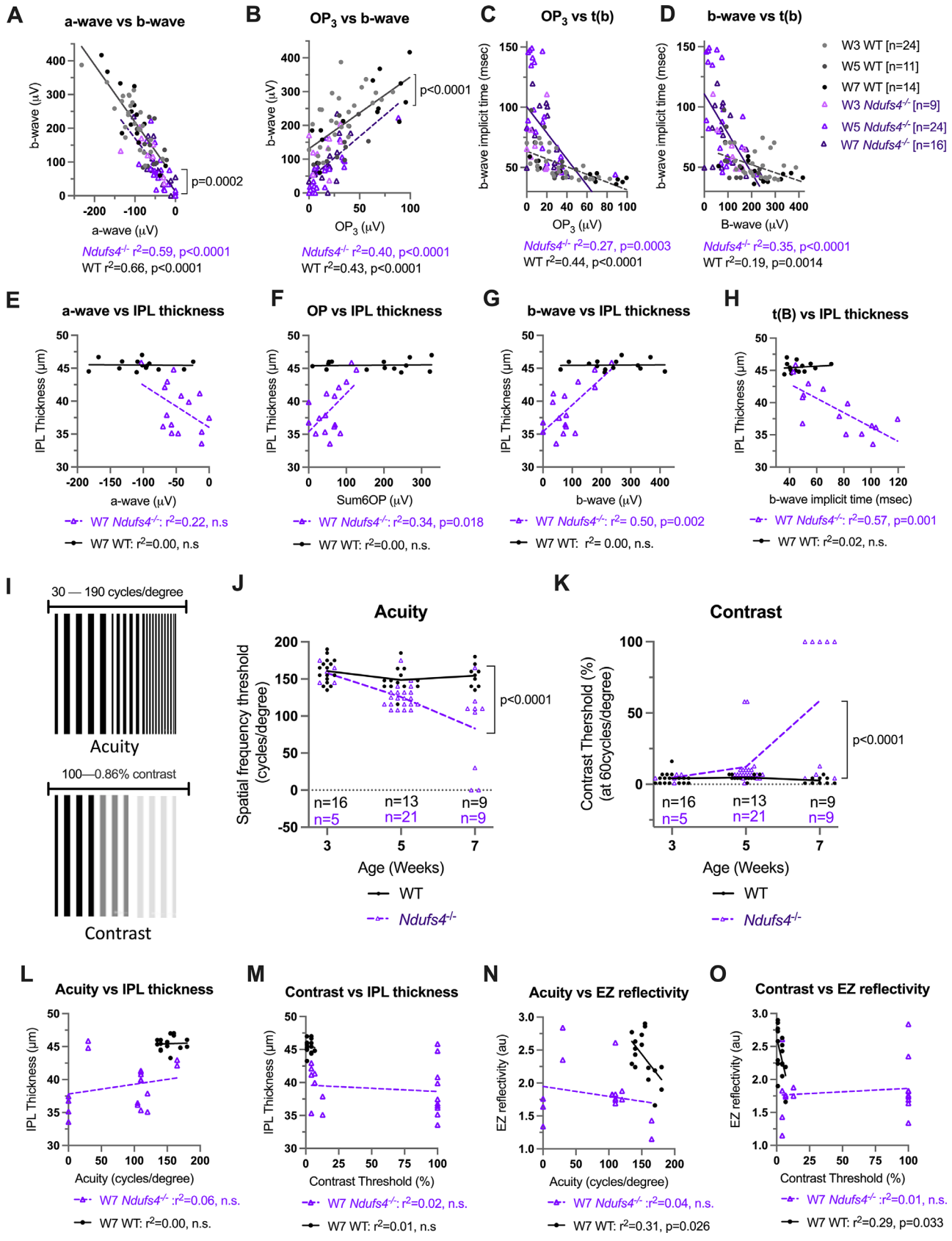

Figure 6. ERG correlates and OMR measures of contrast and acuity perception deficits. (**A**) Linear regression between a- and b-wave amplitudes in WT and *Ndufs4*$^{-/-}$ littermates. (**B**) Linear regression between OP_3 and b-wave amplitudes in WT and *Ndufs4*$^{-/-}$ littermates. →

Downloaded from hwmaint.iovs.org on 04/24/2024

←

(**C**) Linear regression between OP_3 and b-wave implicit time in WT and *Ndufs4*$^{-/-}$ littermates. (**D**) Linear regression between b-wave and b-wave implicit time in WT and *Ndufs4*$^{-/-}$ littermates. (**E**–**H**) Linear regressions between IPL thickness and a-wave amplitude (**E**), OP amplitude (**F**), b-wave amplitude (**G**), and b-wave implicit time (**H**). (**I**) Schematic demonstrating grating patterns with increasing difficulty of acuity or contrast perception. (**J**) Acuity sensitivity threshold (cycles/degree) in WT and *Ndufs4*$^{-/-}$ mice. (**K**) Contrast sensitivity threshold (% contrast) in WT and *Ndufs4*$^{-/-}$ mice (*n* at each timepoint is indicated on the graphs). Data are presented as mean ± SEM. Differences between groups were analyzed by two-way ANOVA, followed by Tukey's multiple comparisons test. Multiple comparisons plots are shown in Supplementary Figure S4. Linear regression between IPL thickness (WT, $n = 18$; *Ndufs4*$^{-/-}$, n = 18) and acuity (**L**) or contrast sensitivity (**M**) at 7 weeks. Linear regression between EZ reflectivity (WT, $n = 18$; *Ndufs4*$^{-/-}$, $n = 18$) and acuity (**N**) or contrast sensitivity (**O**) at 7 weeks.

deficits than expected from the attenuated b-wave or OP_3 amplitudes. Because quantification of b-wave implicit times depends on accurate detection of a b-wave peak, delays in b-wave implicit times may be confounded by poorly defined b-wave responses resulting from either b-wave or OP deficits.

We next investigated whether ERG deficits were correlated with IPL atrophy in 7-week-old animals. IPL atrophy in 7-week-old *Ndufs4*$^{-/-}$ animals was not significantly correlated with a-wave amplitude (Fig. 6E) and was moderately correlated with OP amplitude (Fig. 6F). Meanwhile, both b-wave amplitudes and b-wave implicit times were strongly correlated with IPL atrophy at 7 weeks (Figs. 6G, 6H). Because ERG deficits precede the onset of IPL atrophy, these correlations imply that pathology underlying ERG b-wave dysfunction is related to the drivers of IPL atrophy.

Optomotor Reflex Measure of Acuity and Contrast Sensitivity

Visual acuity and contrast sensitivities were stable in WT animals 3 to 7 weeks of age (Figs. 6I–6K, Supplementary Fig. S4). *Ndufs4*$^{-/-}$ littermates had normal visual function at 3 weeks of age and displayed increasing deficits in both acuity and contrast detection at later ages. In 7-week-old *Ndufs4*$^{-/-}$ animals, acuity sensitivity was 46.6% lower (95% CI, 25.1–68.0) compared to WT littermates, and 56% (five out of nine animals tested) failed to detect any visual stimuli presented at <100% contrast. Because IPL atrophy and visual function deficits appeared on similar timelines, we investigated whether these measures were correlated by linear regression (Figs. 6L, 6M). We found no significant correlations between these readouts. We further investigated if optomotor reflex (OMR) deficits were correlated with EZ hyporeflectivity, as EZ disruption is associated with visual acuity deficits in patients with retinal disease.[28,29] Curiously, acuity and contrast sensitivity were both weakly correlated with EZ reflectivity in WT animals (Figs. 6N, 6O); however, this relationship was absent in *Ndufs4*$^{-/-}$ littermates.

Discussion

The *Ndufs4*$^{-/-}$ mouse model of complex I deficiency exhibits progressive retinal pathology measurable by OCT, ERG, and OMR. These findings build upon existing literature describing the biochemical and cellular underpinnings of retinal pathology in the *Ndufs4*$^{-/-}$ mouse (Fig. 7). Concurrently, physiological retinal remodeling in 3- to 7-week-old WT littermates produces thinning of inner retinal layers, reduction of ELM reflectivity, and attenuation of ERG response.

This temporal profile captures both physiological and pathological retinal changes in recently weaned mice. Murine postnatal retinal development is most pronounced during the first 3 weeks of life; however, physiological and morphological changes persist in 3- to 7-week-old animals.[30,31] These temporal changes require careful age matching of WT and knockout animals to avoid conflating genotype-specific phenotypes with physiological retinal development.

We used both male and female animals and did not observe any overt sex dependence in phenotype; however, many of the observed phenotypes are highly variable, and our studies were not powered to evaluate the effect of sex on *Ndufs4*$^{-/-}$ pathology. Our measurements captured the variability and severity of ocular pathology in differently aged cohorts of *Ndufs4*$^{-/-}$ and WT littermate mice. Additional subtle differences between knockout and WT littermates may be revealed by longitudinal evaluation of individual animals. Further study should evaluate whether differences in the severity of retinal pathology during late stage of disease can be predicted from ocular readouts in younger animals to help reduce the necessary sample sizes for interventional experiments. Our measurements confirm that ERG deficits are present in *Ndufs4*$^{-/-}$ mice at weaning and do not reflect progressive pathology in this model. Conversely, OCT measures of IPL thickness and OMR measures of acuity and contrast sensitivity identified an accelerated period of retinal degeneration in *Ndufs4*$^{-/-}$ animals during weeks 5 to 7.

Downloaded from hwmaint.iovs.org on 04/24/2024

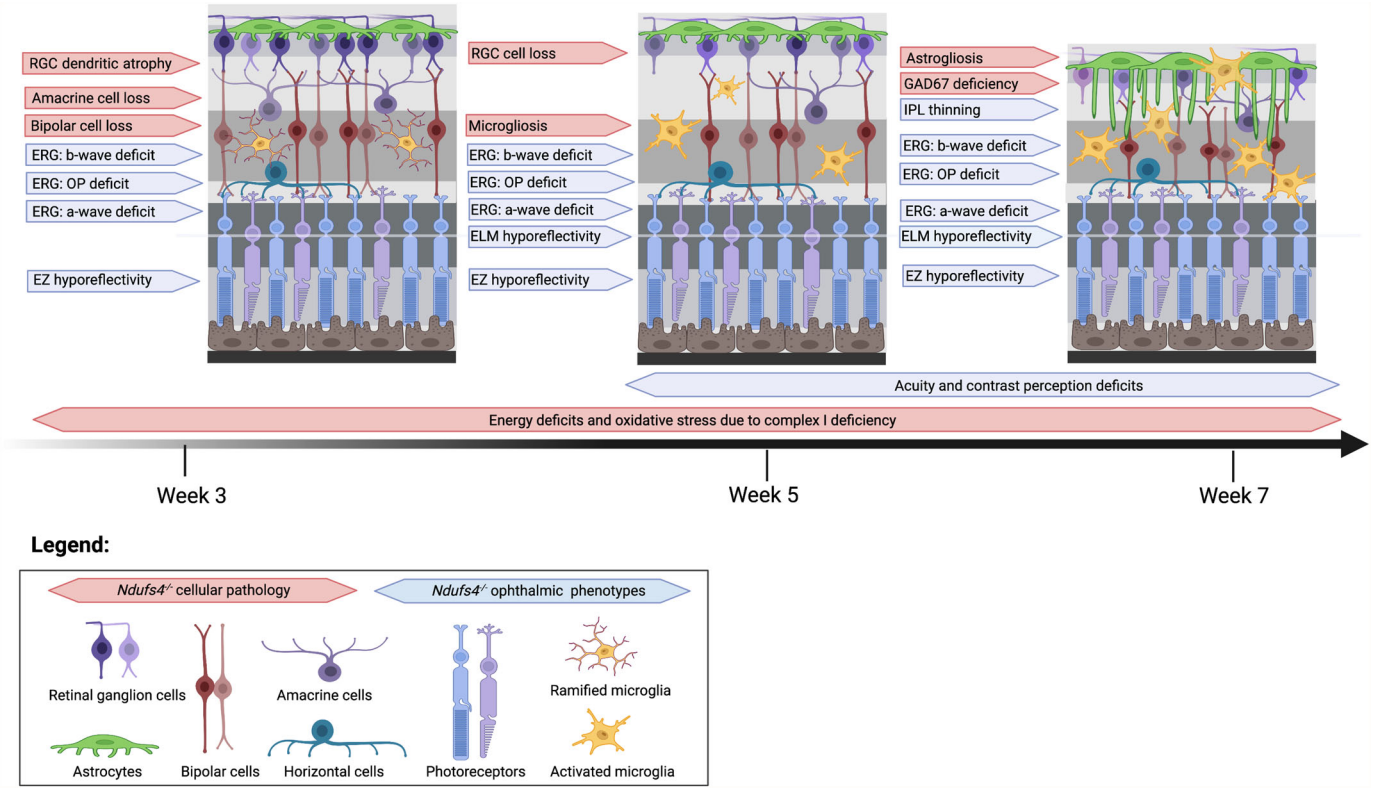

Figure 7. Integrated summary of retinal pathology in *Ndufs4*$^{-/-}$ mouse. Schematic summarizing timeline of retinal pathologies observed in *Ndufs4*$^{-/-}$ mice in published literature and in the present study. ERG impairment secondary to energetic deficits occurred throughout the entire study period (weeks 3–7), and acuity and contrast deficits appeared in 5- to 7-week-old mice. The early phase (week 3) of retinal pathology in *Ndufs4*$^{-/-}$ mice featured RGC dendritic atrophy,[23] amacrine and bipolar cell loss,[19,23] and ELM and EZ hyporeflectivity. At 5 weeks, *Ndufs4*$^{-/-}$ mice exhibited RGC firing deficits,[19] RGC cell loss,[19] and microgliosis.[18,19] During the terminal phase of disease progression (weeks 6–7), *Ndufs4*$^{-/-}$ mice displayed astrogliosis,[11] loss of GAD67 immunoreactivity in IPL,[19] and IPL atrophy. Figure made with Biorender.com.

These measures represent reliable, noninvasive tools for interrogating retinal pathology caused by complex I insufficiency.

Our analysis helps explain discrepancies among previously reported ERG phenotypes in *Ndufs4*$^{-/-}$ animals.[10,11,22] We observed profound ERG deficits in 3-week-old mice, with only minimal progression of impairment in older animals. The highly variable penetrance of ERG deficits, particularly in younger animals, helps explain why some studies failed to detect an ERG deficit in younger mice. Gospe et al.[22] reported that *Ndufs4*$^{-/-}$ photoreceptors are fundamentally capable of normal light-evoked signaling and that deficits in ERG response reflect energetic deficits, rather than a neurodegenerative phenotype. Our findings support this interpretation.

Oscillatory potentials are thought to reflect signaling among bipolar cells, amacrine cells, and ganglion cells.[27] Degeneration of these neuronal populations has been reported in 3-week-old *Ndufs4*$^{-/-}$ retinas.[19,23] It remains unclear whether OP deficits reflect early degeneration of inner retinal neurons or if impaired OP amplitudes also primarily reflect energy deficits.

Amplitude and implicit time measures from ERG waveforms were highly interrelated. ERG b-wave amplitude is influenced by the magnitude of the a-wave negative inflection, and overlapping of OPs with the low-frequency components of the ERG waveform may influence the detection of b-wave peaks.[32] We sought to address some of the potential confounders among different ERG measures by applying correlation analysis. However, there are several limitations to the present study. First, we relied on automated detection of ERG b-wave amplitude and implicit times. This approach did not enable us to eliminate the contribution of differential OP timing and amplitude from the quantification of ERG b-wave parameters. Second, we relied on the image-guided functionality of the MICRON IV Focal ERG System to ensure appropriate illumination of the central retinal fundus. Pupil dilation was not measured, and equal retinal illumination was assumed between groups and ages.

Downloaded from hwmaint.iovs.org on 04/24/2024

Differences in pupil dilation or corneal clarity may result in reduced retinal illuminance and subsequently reduced ERG components and slower implicit times. Third, to support the larger sample sizes evaluated in this study, ERG responses were measured at three distinct illumination intensities, and comparisons between groups were analyzed at the highest intensity measured. This ERG protocol precluded calculation of a luminance–response function, which requires measurements across a broader range of stimulus intensities. These limitations invite future studies to conduct a more thorough examination of ERG deficits in *Ndufs4*$^{-/-}$ mice.

Thinning of the IPL in 5- to 7-week-old *Ndufs4*$^{-/-}$ mice likely reflects atrophy of RGCs, amacrine cells, and bipolar cells.[11,19,20,22] OCT imaging provides a noninvasive and highly reproducible measure of inner retinal degeneration, consistent with reported H&E cross-sections from 7-week-old *Ndufs4*$^{-/-}$ mice.[11] Because IPL atrophy begins at least 2 weeks after weaning, this measure of retinal disease progression is tractable for evaluating pharmacological interventions.

We also observed outer retinal OCT hyporeflectivity in *Ndufs4*$^{-/-}$ mice. Optical density of OCT imaging is highly sensitive to refractive index changes between retinal layers, and the reflectivity of outer retinal bands on OCT imaging is thought to indicate changes in mitochondrial morphology and localization.[33–36] In patients with outer retinal pathologies, EZ hyporeflectivity correlates with visual acuity deficits.[28,29] Similar reflectivity phenotypes have been observed in animal models of photoreceptor light injury[37,38] and retinal oxidative damage.[39,40] Our analysis found correlation between EZ reflectivity and OMR response in WT mice, supporting a relationship between EZ reflectivity and visual function. However, this effect was not observed in *Ndufs4*$^{-/-}$ mice. In hibernating ground squirrels, EZ hyporeflectivity is associated with mitochondrial remodeling during torpor and loss of mitochondria from photoreceptor inner segment region.[33] Thus, it is plausible that outer retinal hyporeflectivity in the *Ndufs4*$^{-/-}$ mouse may reflect abnormalities in mitochondrial distribution and morphology. However, without direct characterization of *Ndufs4*$^{-/-}$ photoreceptor mitochondria, it is challenging to draw a conclusive interpretation of the OCT hyporeflectivity phenotype.

OMR measures progressive visual function deficits in the *Ndufs4*$^{-/-}$ mouse. The optomotor reflex prompts an animal to turn its head in response to a moving visual stimulus. Contrast sensitivity can specifically highlight deficits in retinal function,[41,42] and measures of visual acuity provide a global readout of visual processing by the retina and visual cortex. WT mice 3 to 7 weeks of age had stable acuity and contrast sensitivity scores, whereas *Ndufs4*$^{-/-}$ littermates exhibited marked declines in visual function at weeks 5 to 7. This timeline is consistent with the study by Yu et al.,[18] who reported visual cliff test and slow angled-descent forepaw grasping test deficits in 5-week-old *Ndufs4*$^{-/-}$ mice. Visual function testing by OMR may be less physically demanding compared to alternative tests such as the Morris water maze and the visual cliff test (which demand whole-body movements in response to visual cues). OMR response requires equal levels of minimal physical exertion (head turning) to react to visual stimuli of different difficulties. Thus, OMR testing enables visual function assessment in older, physically weakened animals, allowing monitoring of visual function impairments later into the disease process. Activity levels were not quantified between WT and *Ndufs4*$^{-/-}$ littermate mice and may present a confounding contributor to poor response to OMR stimulus. It should be noted, that 22% (two of nine) of 7-week-old *Ndufs4*$^{-/-}$ mice failed to respond to any visual stimuli during OMR testing. Complete failure to exhibit an OMR response may indicate either complete loss of visual ability or severe neurological or motor function deficits.

Although deletion of *Ndufs4* is most directly related to human Leigh syndrome, deficits in mitochondrial complex I contribute to optic atrophy in several retinal pathologies, including Leber's hereditary optic neuropathy,[2] autosomal dominant optic atrophy,[43] and primary open-angle glaucoma.[44] The *Ndufs4*$^{-/-}$ mouse offers a robust model of ocular pathology from mitochondrial complex I deficiency. The Table summarizes key retinal deficits in *Ndufs4*$^{-/-}$ mice at 3, 5, and 7 weeks of age. Although many pathological features could be detected in younger mice, differences between the WT and knockout groups were more clearly evident in 5- to 7-week-old mice. Due to the severity of retinal pathology, knockout phenotypes can be identified using relatively small sample sizes. Evaluation of potential therapeutic strategies, however, may require significantly larger sample sizes due to variable degrees of impairment among knockout animals. OMR acuity and contrast deficits are highly variable among *Ndufs4*$^{-/-}$ mice and may be challenging readouts for evaluating potential vision-restorative therapies. ELM and EZ reflectivity deficits were similarly highly variable and require further mechanistic study to identify the significance of this phenotype in *Ndufs4*$^{-/-}$ animals. For interventions expected to directly correct complex I activity, ERG responses can be used to detect improvement of retinal phototransduction with sample sizes that are typical

Downloaded from hwmaint.iovs.org on 04/24/2024

for *in vivo* study designs. Alternatively, OCT morphology has low inter-animal variability and is well suited to evaluate neuroprotective interventions aimed at reducing inner retinal atrophy. In sum, ERG, OCT, and OMR measures offer a panel of translatable noninvasive tools for evaluating retinal pathology in the *Ndufs4*$^{-/-}$ model of complex I deficiency.

Acknowledgments

The authors thank Svitlana Avrutsky for helpful feedback on image data analysis.

Supported by grants from the National Institute of Neurological Disorders and Stroke, National Institutes of Health (RO1 NS081333 and R03 NS099920 to CMT) and by the Department of Defense Army Research Office/Air Force Office of Research Defense University Research Instrumentation Program (CMT).

Disclosure: **M.I. Avrutsky**, None; **J.M. Lawson**, None; **J.E. Smart**, None; **C.W. Chen**, None; **C.M. Troy**, None

References

1. Fassone E, Rahman S. Complex I deficiency: clinical features, biochemistry and molecular genetics. *J Med Genet*. 2012;49:578–590.
2. Stenton SL, Sheremet NL, Catarino CB, et al. Impaired complex I repair causes recessive Leber's hereditary optic neuropathy. *J Clin Invest*. 2021;131:e138267.
3. Lake NJ, Compton AG, Rahman S, Thorburn DR. Leigh syndrome: one disorder, more than 75 monogenic causes. *Ann Neurol*. 2016;79:190–203.
4. González-Rodríguez P, Zampese E, Stout KA, et al. Disruption of mitochondrial complex I induces progressive parkinsonism. *Nature*. 2021;599:650–656.
5. Surmeier DJ, Obeso JA, Halliday GM. Selective neuronal vulnerability in Parkinson disease. *Nat Rev Neurosci*. 2017;18:101–113.
6. Logan R, Dubel-Haag J, Schcolnicov N, Miller SJ. Novel genetic signatures associated with sporadic amyotrophic lateral sclerosis. *Front Genet*. 2022;13:851496.
7. Brandt U. Energy converting NADH:quinone oxidoreductase (complex I). *Annu Rev Biochem*. 2006;75:69–92.
8. Mimaki M, Wang X, McKenzie M, Thorburn DR, Ryan MT. Understanding mitochondrial complex I assembly in health and disease. *Biochim Biophys Acta*. 2012;1817:851–862.
9. Ugalde C, Janssen RJ, van den Heuvel LP, Smeitink JA, Nijtmans LG. Differences in assembly or stability of complex I and other mitochondrial OXPHOS complexes in inherited complex I deficiency. *Hum Mol Genet*. 2004;13:659–667.
10. Kruse SE, Watt WC, Marcinek DJ, Kapur RP, Schenkman KA, Palmiter RD. Mice with mitochondrial complex I deficiency develop a fatal encephalomyopathy. *Cell Metab*. 2008;7:312–320.
11. Jiang D, Xiong G, Feng H, et al. Donation of mitochondria by iPSC-derived mesenchymal stem cells protects retinal ganglion cells against mitochondrial complex I defect-induced degeneration. *Theranostics*. 2019;9:2395–2410.
12. Kahlhöfer F, Kmita K, Wittig I, Zwicker K, Zickermann V. Accessory subunit NUYM (*NDUFS4*) is required for stability of the electron input module and activity of mitochondrial complex I. *Biochim Biophys Acta Bioenerg*. 2017;1858:175–181.
13. Leong DW, Komen JC, Hewitt CA, et al. Proteomic and metabolomic analyses of mitochondrial complex I-deficient mouse model generated by spontaneous B2 short interspersed nuclear element (SINE) insertion into NADH dehydrogenase (ubiquinone) Fe-S protein 4 (*Ndufs4*) gene. *J Biol Chem*. 2012;287:20652–20663.
14. Anderson SL, Chung WK, Frezzo J, et al. A novel mutation in *NDUFS4* causes Leigh syndrome in an Ashkenazi Jewish family. *J Inherit Metab Dis*. 2008;31(suppl 2):S461–S467.
15. Leshinsky-Silver E, Lebre AS, Minai L, et al. *NDUFS4* mutations cause Leigh syndrome with predominant brainstem involvement. *Mol Genet Metab*. 2009;97:185–189.
16. Lamont RE, Beaulieu CL, Bernier FP, et al. A novel *NDUFS4* frameshift mutation causes Leigh disease in the Hutterite population. *Am J Med Genet A*. 2017;173:596–600.
17. González-Quintana A, Trujillo-Tiebas MJ, Fernández-Perrone AL, et al. Uniparental isodisomy as a cause of mitochondrial complex I respiratory chain disorder due to a novel splicing *NDUFS4* mutation. *Mol Genet Metab*. 2020;131:341–348.
18. Yu AK, Datta S, McMackin MZ, Cortopassi GA. Rescue of cell death and inflammation of a mouse model of complex 1-mediated vision loss

Downloaded from hwmaint.iovs.org on 04/24/2024

by repurposed drug molecules. *Hum Mol Genet*. 2017;26:4929–4936.
19. Yu AK, Song L, Murray KD, et al. Mitochondrial complex I deficiency leads to inflammation and retinal ganglion cell death in the *Ndufs4* mouse. *Hum Mol Genet*. 2015;24:2848–2860.
20. Reynaud-Dulaurier R, Benegiamo G, Marrocco E, et al. Gene replacement therapy provides benefit in an adult mouse model of Leigh syndrome. *Brain*. 2020;143:1686–1696.
21. Indrieri A, Carrella S, Romano A, et al. miR-181a/b downregulation exerts a protective action on mitochondrial disease models. *EMBO Mol Med*. 2019;11:e8734.
22. Gospe SM, 3rd, Travis AM, Kolesnikov AV, et al. Photoreceptors in a mouse model of Leigh syndrome are capable of normal light-evoked signaling. *J Biol Chem*. 2019;294:12432–12443.
23. Song L, Yu A, Murray K, Cortopassi G. Bipolar cell reduction precedes retinal ganglion neuron loss in a complex 1 knockout mouse model. *Brain Res*. 2017;1657:232–244.
24. Avrutsky MI, Ortiz CC, Johnson KV, et al. Endothelial activation of caspase-9 promotes neurovascular injury in retinal vein occlusion. *Nat Commun*. 2020;11:3173.
25. Benkner B, Mutter M, Ecke G, Münch TA. Characterizing visual performance in mice: an objective and automated system based on the optokinetic reflex. *Behav Neurosci*. 2013;127:788–796.
26. Yu DY, Cringle SJ, Balaratnasingam C, Morgan WH, Yu PK, Su EN. Retinal ganglion cells: energetics, compartmentation, axonal transport, cytoskeletons and vulnerability. *Prog Retin Eye Res*. 2013;36:217–246.
27. Creel DJ. Electroretinograms. *Handb Clin Neurol*. 2019;160:481–493.
28. Gu J, Jiang T, Yu M, et al. A novel approach to quantitative evaluation of outer retinal lesions via a new parameter "integral" in spectral domain optical coherence tomography. *Transl Vis Sci Technol*. 2020;9:8.
29. Guyon B, Elphege E, Flores M, Gauthier AS, Delbosc B, Saleh M. Retinal reflectivity measurement for cone impairment estimation and visual assessment after diabetic macular edema resolution (RECOVER-DME). *Invest Ophthalmol Vis Sci*. 2017;58:6241–6247.
30. Fan J, Jia L, Li Y, et al. Maturation arrest in early postnatal sensory receptors by deletion of the miR-183/96/182 cluster in mouse. *Proc Natl Acad Sci USA*. 2017;114:E4271–E4280.
31. Augustin M, Wechdorn M, Pfeiffenberger U, et al. In vivo characterization of spontaneous retinal neovascularization in the mouse eye by multifunctional optical coherence tomography. *Invest Ophthalmol Vis Sci*. 2018;59:2054–2068.
32. Gao M, Barboni MTS, Ventura DF, Nagy BV. Effects of fixed cutoff filtering on dark- and light-adapted ERG components and the application of variable cutoff filter. *Doc Ophthalmol*. 2022;144:191–202.
33. Sajdak BS, Bell BA, Lewis TR, et al. Assessment of outer retinal remodeling in the hibernating 13-lined ground squirrel. *Invest Ophthalmol Vis Sci*. 2018;59:2538–2547.
34. Ross DH, Clark ME, Godara P, et al. RefMoB, a reflectivity feature model-based automated method for measuring four outer retinal hyperreflective bands in optical coherence tomography. *Invest Ophthalmol Vis Sci*. 2015;56:4166–4176.
35. Litts KM, Zhang Y, Freund KB, Curcio CA. Optical coherence tomography and histology of age-related macular degeneration support mitochondria as reflectivity sources. *Retina*. 2018;38:445–461.
36. Sajdak BS, Salmon AE, Cava JA, et al. Noninvasive imaging of the tree shrew eye: wavefront analysis and retinal imaging with correlative histology. *Exp Eye Res*. 2019;185:107683.
37. Miller EB, Zhang P, Ching K, Pugh EN, Jr, Burns ME. In vivo imaging reveals transient microglia recruitment and functional recovery of photoreceptor signaling after injury. *Proc Natl Acad Sci USA*. 2019;116:16603–16612.
38. Zhong X, Aredo B, Ding Y, Zhang K, Zhao CX, Ufret-Vincenty RL. Fundus camera-delivered light-induced retinal degeneration in mice with the RPE65 Leu450Met variant is associated with oxidative stress and apoptosis. *Invest Ophthalmol Vis Sci*. 2016;57:5558–5567.
39. Hariri S, Moayed AA, Choh V, Bizheva K. In vivo assessment of thickness and reflectivity in a rat outer retinal degeneration model with ultrahigh resolution optical coherence tomography. *Invest Ophthalmol Vis Sci*. 2012;53:1982–1989.
40. Zhang N, Zhang X, Girardot PE, et al. Electrophysiologic and morphologic strain differences in a low-dose $NaIO_3$-induced retinal pigment epithelium damage model. *Transl Vis Sci Technol*. 2021;10:10.
41. Xiao J, Adil MY, Chang K, et al. Visual contrast sensitivity correlates to the retinal degeneration in rhodopsin knockout mice. *Invest Ophthalmol Vis Sci*. 2019;60:4196–4204.
42. Khani MH, Gollisch T. Diversity in spatial scope of contrast adaptation among mouse retinal ganglion cells. *J Neurophysiol*. 2017;118:3024–3043.

Downloaded from hwmaint.iovs.org on 04/24/2024

43. Van Bergen NJ, Crowston JG, Kearns LS, et al. Mitochondrial oxidative phosphorylation compensation may preserve vision in patients with OPA1-linked autosomal dominant optic atrophy. *PLoS One*. 2011;6:e21347.

44. Lee S, Sheck L, Crowston JG, et al. Impaired complex-I-linked respiration and ATP synthesis in primary open-angle glaucoma patient lymphoblasts. *Invest Ophthalmol Vis Sci*. 2012;53:2431–2437.

Downloaded from hwmaint.iovs.org on 04/24/2024